# Helicopter Rotor Ground Effect and Frigate Interaction Investigated by Particle Image Velocimetry

Rafael Bardera Mora* and Juan Carlos Matías García†
*National Institute for Aerospace Technology, 28850 Torrejón de Ardoz, Spain*

**Helicopter maneuvers on frigates develop an essential role during military operations. However, the complex flow generated by the frigate bluff-body shapes and the interaction with the helicopter downwash during the recovery process must be studied in detail. In addition, the ground effect can also affect helicopter performance during the maneuver. This study aims to use Particle Image Velocimetry (PIV) in wind tunnel to analyze the airflow generated by a 1:100 scaled helicopter rotor of the Sea King SH-3 navy helicopter isolated and with the presence of a full and a partial ground to consider the ground effect at different heights. Once the rotor has been studied, experimental tests were carried out of the rotor working next to a frigate model during the recovery maneuver. The measured velocity indicates that the flow asymmetry below the rotor can increase with the proximity to a partial ground distance up to 1.39 times. During the study of the rotor for the frigate landing approach, the downwash asymmetry is also important and changes abruptly the tendency during the last phase of the maneuver. It can lead to dangerous instabilities and problems for the helicopter pilot during the hovering over ships.**

## I. Nomenclature

A = Asymmetry parameter

$A_L$ = Area under the velocity profiles of the left part of the rotor downwash

$A_R$ = Area under the velocity profiles of the right part of the rotor downwash

$a$ = Coefficient for velocity values of Hiemenz flow

Presented at as Paper 2020-2740 at the AIAA Aviation Forum 2020, 15–19 June 2020, VIRTUAL EVENT
* PhD Aerospace Engineer. Experimental Aerodynamics, Madrid; barderar@inta.es
† Aerospace Engineer, Experimental Aerodynamics, Madrid; matiasgjc@inta.es

$c$ = Blade profile chord (m)

$C_P$ = Power coefficient

$C_Q$ = Torque coefficient

$C_T$ = Thrust coefficient

$D$ = Rotor diameter (m)

$h$ = Height above the ground of the rotor (m)

$J$ = Rotor inflow ratio

$M$ = Camera magnification of the PIV system

$M_{tip}$ = Mach number at the rotor tip

$N$ = Blade number

$P_{io}$ = Induced power of the rotor during hovering flight (W)

$Q_{io}$ = Rotor torque during hovering flight (N·m)

$R$ = Rotor radius (m)

$Re_c$ = Reynolds number of the rotor model based on the chord length

$r, z$ = radial ($r$) and vertical ($z$) axial coordinates in millimeters (mm)

$S$ = Rotor area ($m^2$)

$T_{io}$ = Rotor thrust during hovering flight (N)

$u_{PIV}$ = PIV uncertainty

$v_{io}(r)$ = Induced axial velocity measured at a differential point in a radial coordinate (r) (m/s)

$V_{io}$ = Mean induced axial velocity at the disc plane during hovering flight (m/s)

$v_{tip}$ = Blade tip velocity (m/s)

$V_z$ = Axial velocity (m/s)

$W$ = Helicopter Weight (kg)

$\mu$ = Advance Ratio

$\rho$ = Air density ($kg/m^3$)

$\Omega_{fs}$ = Angular velocity of the helicopter full-scale rotor (rad/s)

$\Omega_m$ = Angular velocity of the helicopter rotor model (rad/s)

ABBREVIATIONS:

CFD = Computational Fluid Dynamics

INTA = National Institute of Aerospace Technology

LES = Large Eddy Simulation

PIV = Particle Image Velocimetry

rpm = Revolutions per minute

SFS = Simplified Frigate Shape

SRM = Steady Rotor Model

URANS = Unsteady Reynolds-averaged Navier-Stokes

USRM = Unsteady rotor model

## II.Introduction

Helicopter flight around ships involves complex and risky operations for the pilots. When the pilots must perform the final approach and landing maneuver on a frigate flight deck, the flow where the helicopter is immersed is affected by high-velocity gradients and turbulence levels. The pilot workload is increased because he has to constantly correct the aircraft trajectory and the flight controls. This makes helicopter landing on frigates a risky maneuver that must be studied to ensure safety for the pilot.

Different authors have presented experimental and numerical studies related to the problem of aircraft and ship aerodynamic interference when they are operating closely. Good examples of learning the flow around a bluff-body shape such as a frigate are included in [1-3]. They explain the main problems presented around a ship for the helicopter performance.

In the field of numerical simulation, there are a lot of Computational Fluid Dynamic (CFD) studies that analyze the airflow around frigates [4] and their interaction with the helicopter performance [5]. Barakos et al. [6] carried out CFD simulations to study the rotor aerodynamic effect when it is operating around a ship superstructure. Steady and unsteady Reynolds-averaged Navier-Stokes (URANS) equations with a fully-articulated rotor blade model were used. The results showed that a rotor which is operating around a frigate makes it impossible to solve the problem by superposition methods. To analyze the increase in pilot workload during helicopter maneuvers around frigates, Foeken

and Pavel [7] presented a paper to propose models and simulations of rotor flow, ground effect, ship motion, and pilot modeling to increase fidelity in the simulation of helicopter and ship operations, reducing the number of expensive flight tests [8-10]. A CFD model of a hovering helicopter was presented by Wakefield et. al. [2] to find the required power and pitch to maintain the hovering condition in that situation. Steady RANS and hybrid RANS-Large Eddy Simulation (LES) CFD studies were conducted for obtaining useful data for simulating the helicopter-ship interaction in a flight simulator [11]. Another numerical study [12] was developed with a Navier-Stokes solver, steady rotor model (SRM) and unsteady rotor model (URM). Different numerical models (PANS and LES simulations) were used by Zhang et al. [13]. Other comparison between numerical and experimental data for a static frigate including turbulence distributions under different wind angle conditions can be found in [14].

There are more specific CFD studies related to the combined problem of the frigates airwake and the helicopter rotor operations around them [15]. For example, Ji et al. [16] generated a real-time simulation model for the analysis of helicopter recovery maneuvers during turbulent atmospheric environment conditions. Forsythe et al. [17] made a fully coupled hovering simulation of the rotorcraft and ship airwake to analyze numerically the helicopter approach to a ship. Trying to improve the flow above the flight deck of a frigate and make the helicopter operations safer by reducing the pilot workload levels, Forrest et al. [18] tested five hangar-edge modifications through CFD simulation. In a more recent study [19] the same authors analyzed again the hangar-edge configurations by means of flight trials in a motion-base simulator.

As the frigate and helicopter interference is a common field of interest in aerodynamic research, there are also experimental studies related to the helicopter operation near frigates. A first example of experimental results is the Laser Doppler Anemometry measurements made by Bardera et al. [20]. They were made in order to analyze the turbulence levels in five points of a helicopter landing trajectory on a frigate. The results were compared against full-scale frigate measurements. In a water tunnel, Kääriä et al. [21] measured the aerodynamic loading of a Merlin AW-101 1:50 model-scale helicopter operating in the air wake of a generic frigate ship. They obtained the forces by means of a six-component balance integrated inside the helicopter fuselage under headwind and 45º wind-angle conditions. The measured unsteady aerodynamic forces, their effects on the pilot workload and the control input strategies during the landing maneuver were analyzed. Other experimental investigations [22, 23] were conducted on an amphibious ship and 1:48 scaled powered models of helicopters and tiltrotors. The goal was to measure the aerodynamic interaction between the aircraft and the ship using Particle Image Velocimetry (PIV). In 2012, Stargel and Landman

[24] presented another experimental study in a wind tunnel with PIV that analyzed the interaction between a naval frigate and a scaled rotor model. They quantified the coupling levels between the rotor and air wake flowfields. The last example of this type of studies is the measurement of unsteady forces in a helicopter fuselage [25]. They are related to increase workload of the pilot that is performing the landing maneuver on a frigate. Lee and Zan performed wind tunnel tests to measure unsteady aerodynamic loads in a Sea King helicopter fuselage immersed in the air wake of its rotor and the Canadian Patrol Frigate.

With similar to the above-mentioned experimental studies, the aim of this paper is to use experimental data obtained by Particle Image Velocimetry (PIV) during wind tunnel testing to analyze the airflow of a helicopter rotor. This rotor represents a 1:100 scaled rotor model of the helicopter Sea King SH-3, widely used in military naval operations. The rotor will be analyzed working in a free-condition (no ground), close to the ground at different heights and over a frigate flight deck during the last phase of the landing approach. With all the velocity data obtained, parameters such as averaged induced velocities and the asymmetries will be quantified for the rotor model. Curves that relate the ground-effect, the deflection of the downwash produced by the presence of a nearby ground or the flow asymmetries presented in the rotor when it hovers part over the frigate and part over the sea will be analyzed. The pilot workload can be assumed to be higher the greater the flow asymmetries detected in the flow, because the rotor trimming and its changes with time will be more complex for the pilot. The study pretends to be fundamental since no fuselage is present during the generic cases tested. The reason is that the fuselage presence would be a problem for PIV experiments and extracting quality velocity data under the rotor.

Before closing the introduction section, basic equations and a description of the flow during the ground effect of a rotor are going to be described to facilitate the correct understanding of the paper. The mathematical problem of a helicopter rotor can be described using the momentum theory and can be easily found in the literature such as, for example, in Leishman's book [26]. The thrust ($T_{io}$), power ($P_{io}$) and torque ($Q_{io}$), and their associated non-dimensional coefficients ($C_T, C_P, C_Q$) during hovering or stationary flight in a helicopter ($T_{io} = W$) can be defined as,

$$T_{io} = W = 2\rho S V_{io}^2 \quad ; \quad C_T = \frac{T_{io}}{\rho(\Omega R)^2 S} \tag{1}$$

$$P_{io} = T_{io} V_{io} \quad ; \quad C_P = \frac{P_{io}}{\rho(\Omega R)^3 S} \tag{2}$$

$$Q_{io} = \frac{P_{io}}{\Omega} \quad ; \quad C_Q = \frac{Q_{io}}{\rho(\Omega R)^2 R S} \tag{3}$$

where $W$ is the helicopter weight, $\rho$ is the air density, $S$ is the surface of the rotor, $V_{io}$ is the axial induced velocity at the disk plane and Ω is the angular velocity of the rotor. If the axial velocities are known, the thrust can be obtained as,

$$T_{io} = \int_0^R 2\rho S v_{io}^2(r)\, dr = 4\pi\rho \int_0^R v_{io}^2(r)\, r dr \tag{4}$$

where $v_{io}(r)$ is the induced velocity measured at a differential point in a radial coordinate $(r)$. Finally, using equation (1), the mean axial velocity at the disk plane can be easily obtained as,

$$V_{io} = \sqrt{\frac{T_{io}}{2\rho S}} \tag{5}$$

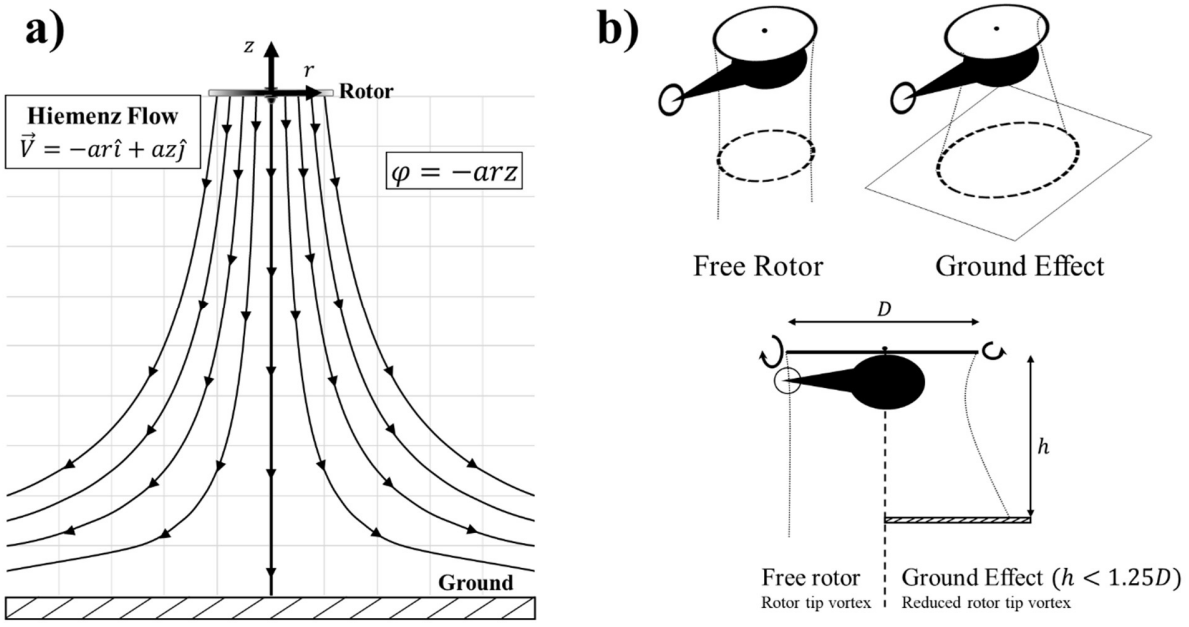



**Fig. 1 a) Streamlines in a Hiemenz flow b) Ground effect in a helicopter rotor**

The momentum theory is not applicable when the rotor is hovering near the ground. The most simplified flow that can represent the resultant flow generated by a rotor near the ground is the Hiemenz flow or stagnation point flow, Figure 1a. This flow consists of air approaching a surface and dividing the flow into two different directions, similar when the air is boosted by the rotor and impact with the ground downstream. Hiemenz flow assumes planar, laminar, inviscid, and incompressible flow. It is a simplified case that has an exact solution for the velocity ($\vec{V}$), and for the potential $\phi$ and streamlines function $\varphi$,

$$\vec{V} = -ar\hat{\imath} + az\hat{\jmath} \tag{6}$$

In addition to the change in flow direction and the existence of a stagnation point, the flow under a helicopter rotor near a wall has another important effect, known as the ground-effect, Figure 1b. The ground-effect is produced when the helicopter rotor is working at a height above ground ($h$) of less than 1.25 diameters ($D$) [26]. It increases the rotor performance due to two different phenomena. The first effect is the reduction of the induced airflow velocity and the increase of the angle of attack. It produces a bigger vertical lift vector for the blades. Which means less power is required to maintain the hovering condition. The second effect is the reduction of the rotor tip vortex that makes the outboard portion of the blades more efficient. To quantify the effect, at a rotor height of one and a half rotor diameter over the ground, the thrust can be increased by 7 %.

## III.Experimental Set-up

### A. Wind Tunnel and Particle Image Velocimetry (PIV)

Experimental tests have been carried out in the wind tunnel T1 test facilities at INTA, Figure 2. The experimental aerodynamics department has a closed circuit and low-speed wind tunnel with an elliptic test section of 3 × 2 $m^2$. It has an engine of 450 kW and can reach velocities up to 60 m/s with low turbulence intensity. In order to obtain velocity maps of the flow at the test section, a Particle Image Velocimetry (PIV) system is used. PIV [27-30] is an advanced velocity measurement technique that needs seeding of the flow with small tracer particles. The particles can be, for example, atomized olive oil tracer particles, with a maximum size of 1 μm. Their small size allows them to properly follow the flow. In order to generate them, Laskin atomizers were used [31, 32]. Another requirement for the proper working of PIV is a powerful laser light source. At INTA, there are two Nd: YAG pulsed lasers with 190 mJ of energy per pulse. Once the light reaches a particle seeded in the flow, the light scatters in all directions. At that moment, a 2048 × 2048 pixels CCD camera equipped with a 50 mm Nikon lens captures two photographs where the particles are visible due to the laser light. Then, their positions are recorded in two different photographs, separated by a very short period of time, $\Delta T = 125$ μs for the tests. Finally, a cross-correlation of small interest windows (32 × 32 pixels) can be made using the Fast Fourier Transform (FFT). In the position where the cross-correlation finds a maximum, it is where the particles of that window have moved in average. Having this displacement $\Delta X$, and as the time between the

laser pulses is known $\Delta T$, the velocity of the particles on each window can be obtained. The process of image capturing and cross-correlation process is made with the INSIGHT3G commercial software.

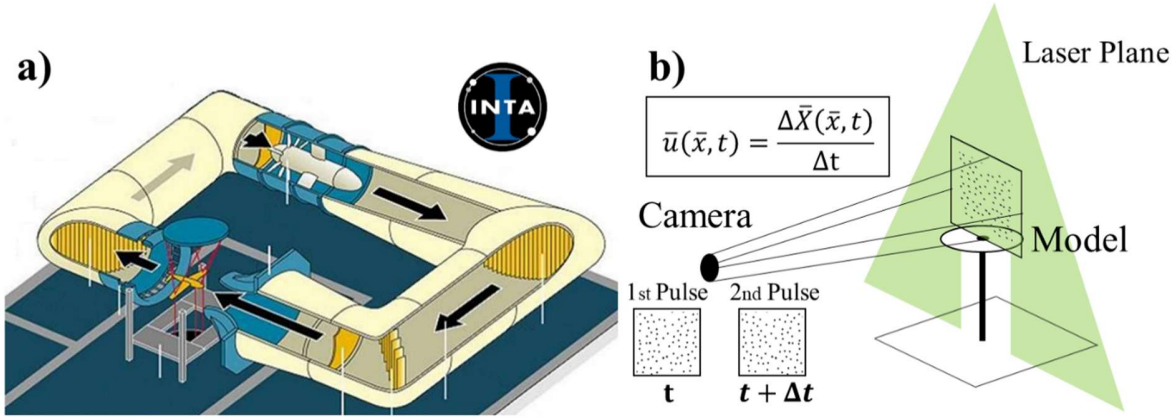



**Fig. 2 Scheme of the Wind Tunnel T1 INTA (a) and Particle Image Velocimetry (b).**

The PIV parameters selected for obtaining velocity maps of the flow were laser pulse delay (between the first frame and the first laser pulse) of 400 μs, pulse separation of 125 μs and PIV exposure of 415 μs. 100 averaged pairs of images were used for each case with the maximal data rate of 10 Hz. Finally, post-processing was applied. Specifically, a gaussian peak fit and 3 × 3 neighbors mean filter was used. In order to represent the non-dimensional velocity maps, Tecplot360 commercial software was used. Finally, taking into account the uncertainty of PIV algorithm estimated as 0.1 pix according [30], uncertainty estimation of the velocity vector from the cross-correlation process used for the tests has been calculated as,

$$u_{PIV} = \frac{0.1}{M\Delta t} = \frac{0.1}{4.09 \times 10^3 \times 125 \times 10^{-6}} = 0.195 \text{ m/s} \tag{7}$$

It means that the uncertainty value is around 1.95 % for 10 m/s velocity vectors. It is important to know that PIV has additional sources of uncertainty related to the equipment and to the particle lag [30]. Finally, the magnification factor ($M$) used for the tests is,

$$M = \frac{CCD\ resolution}{Field\ of\ View} = \frac{2048\ pixels}{500\ mm} = 4.09\ pixels/\text{mm} \tag{8}$$

**B. Rotor Model**

The rotor model used is based on a 1:100 scaled Sikorsky Sea King SH-3 helicopter rotor. The main characteristics of the full-scale rotor and scaled rotor model are displayed in Table 1.

**Table 1 Full-scale rotor and scaled-rotor model characteristics**

| | Name | Full-Scale (fs) | Scaled (m) |
|---|---|---|---|
| N | Blades number | 5 | 5 |
| D | Rotor diameter | 16 m | 0.16 m |
| R | Rotor radius | 8 m | 0.08 m |
| c | Blade profile chord | 0.46 m | 0.02 m |
| $V_{io}$ | Mean induced velocity at the disc plane (hovering condition) | 14.11 m/s | 7 m/s |
| Ω | Rotation speed | 200 rpm | 9,700 rpm |

The rotor model has been built in plastic by additive manufacturing. It is rigid and does not represent the same flexibility as the full-scale rotor. The rotor blades use a NACA 0012 profile. Their blades have a linear torsion of 12º at the root (base) and 6.5º at the blade tip. Note that the geometrical similarity is not completely respected with a blade profile chord of the scaled rotor that is not 100 times smaller. This is done because such a small chord in the 1:100 scaled rotor would present manufacturing complexity and structural problems during high rotation speeds. But this study does not pretend to achieve the fully geometric similarity between the real model and the scale model. Taking this into account, to ensure the flow similarity between the real and scaled rotor model it is essential to meet the similarity based on the thrust coefficient ($C_T$) and the inflow ratio ($J$),

$$J = V_{io}/v_{tip} \tag{9}$$

where $V_{io}$ is the induced velocity below the rotor and $v_{tip} = \Omega R$ is the velocity of the blades tip. By making equal the ratio between the inflow ratios of full-scale and model cases,

$$\frac{J_{fs}}{J_m} = \frac{\left(V_{io}/v_{tip}\right)_{fs}}{\left(V_{io}/v_{tip}\right)_m} = \frac{\left(V_{io_{fs}}/\Omega_{\mathrm{fs}} R_{fs}\right)}{\left(V_{io_m}/\Omega_{\mathrm{m}} R_m\right)} = 1 \tag{10}$$

where $J_{f_s} = 0.067$, $v_{io_{fs}} = 14.11$ m/s, $\Omega_{\mathrm{fs}} = 200$ rpm $= 20.9$ rad/s, $R_{fs} = 8$ m, and $R_m = 0.08$ m. There is a linear dependency relationship to meet the similarity of inflow ratios, $v_{io_m}/\Omega_{\mathrm{m}} = 0.009$.

In preliminary tests of the rotor with a similar experimental set-up it was verified that for an angular velocity of the scaled rotor $\Omega_{\mathrm{m}} = 9{,}700$ rpm, an $v_{io_m} = 7$ m/s measured below the rotor can satisfy the previous linear relationship and therefore fulfill the required similarity of the inflow ratios. When this inflow ratio similarity is

ensured, the thrust coefficient similarity is guaranteed since both parameters are matched with the following expression,

$$T_{io} = 2\rho S V_{io}^2 = \rho(\Omega R)^2 S C_T \quad \rightarrow \quad V_{io}^2 = \frac{(\Omega R)^2 C_T}{2} \quad \rightarrow \quad \left(\frac{V_{io}}{\Omega R}\right)^2 = \frac{C_T}{2} = J^2 \tag{11}$$

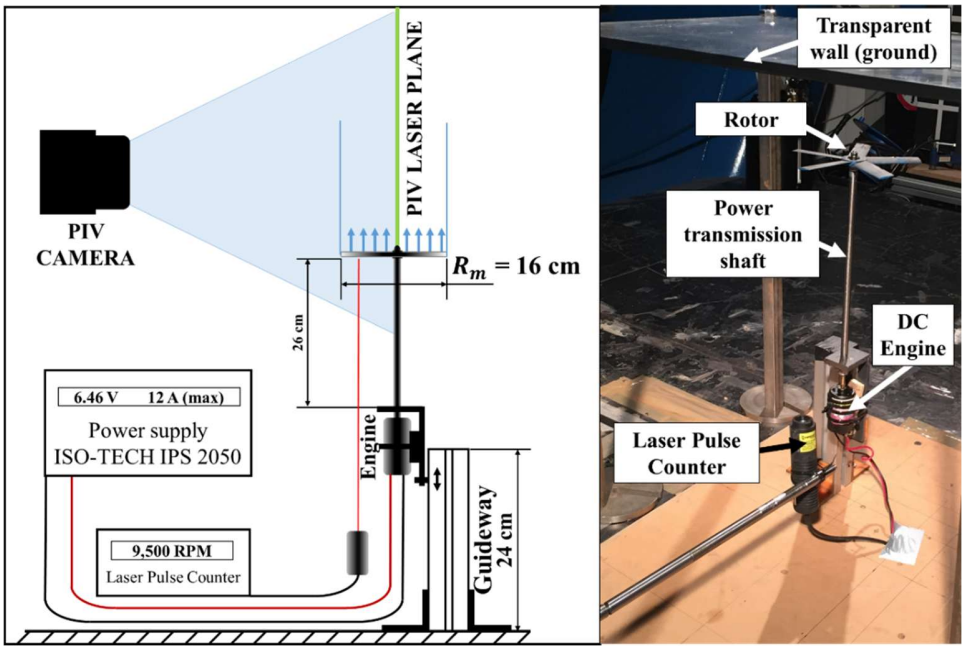



**Fig. 3 Rotor assembly diagram and experimental set-up of the rotor**

At the experimental tests and for controlling the rotational speed of the rotor, the DC engine was connected to a programmable power supply model ISO-TECH IPS 2050, adjustable in voltage and intensity. The engine used, model JAMARA Venti 600 CE, can operate up to 7.2 V, 12 A and 17,500 rpm. The intensity was limited to a maximum value of 12 A and the voltage was selected to 6.46 V to achieve the rotational speed desired of 9,500-10,000 rpm. This rotational speed was controlled during all tests with a laser pulse counter.

Once operating parameters for the rotor model have been defined to fulfill the flow similarity, the Reynolds number based on the profile chord of the rotor model is $Re_c = 1.1 \cdot 10^5$. This Reynolds number is obtained with a tip velocity of the rotor $v_{tip_m} = \Omega_m R_m = 81.3$ m/s, that corresponds to a Mach number at the tip of $M_{tip_m} = 0.24$, that is under 0.3 value, when the compressible effects start to be not negligible. From the similarity of the flow model used, the thrust coefficient is the same for the model and the full-scale rotor ($C_T = 1.5 \cdot 10^{-2}$).

Finally, for all Particle Image Velocimetry (PIV) tests, the scaled rotor was installed on an inverted position, Figure 3. This allows the laser light to illuminate the accelerated flow region under the rotor, where the induced velocity $v_{io}(r)$ appears.

The rotor was attached to the DC engine using a power transmission shaft with a length of 26 cm. The engine was fixed by means of a steel frame to a small vertical guideway which allowed to regulate the rotor height easily during the tests. Finally, the guideway was attached to the wind tunnel test section floor with steel brackets.

### C. Free Isolated Rotor

The first tests were made to obtain the flow above and below the rotor when the rotor is working in free flow without velocity, external disturbances or walls nearby. For that purpose, the rotor was placed in a room at a minimum distance of a wall of 4 meters and a height of the rotor of more than 1 m to the laboratory floor. In all tests, the position and field of view of the camera were maintained.

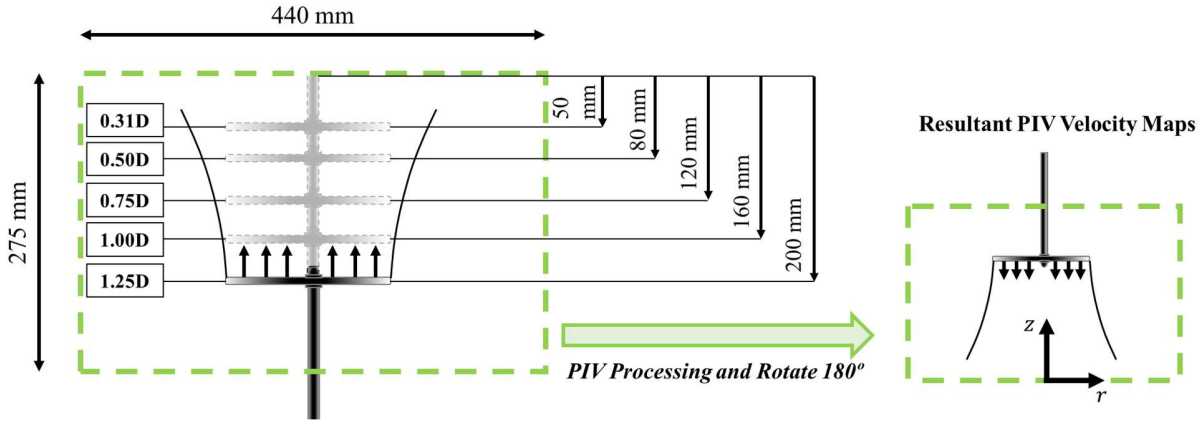



**Fig. 4 Diagram of free isolated rotor PIV tests performed.**

Only the rotor was moved changing its height to obtain all the positions desired, Figure 4. The rotor heights tested in respect to the upper boundary of the camera field of view were 200 mm, 160 mm, 120 mm, 80 mm and 50 mm, which corresponds to 1.25D, 1D, 0.75D, 0.5D and 0.31D. The 50 mm case (5 m at full-scale) corresponds the height where a helicopter rotor hovers when performing the landing maneuver on a frigate. Although in these cases there is no interference with a nearby object, all positions were tested in order to compare these maps directly with those obtained by placing a wall near the rotor at a later stage of the tests.

### D. Rotor-wall interaction

In order to study the rotor and wall aerodynamic interaction, the scaled rotor was tested with a transparent wall made of methacrylate, of 3.2D edge length. This wall was fixed to the upper position of the camera field of view, Figure 5. Again, the rotor was placed at the same heights with respect to the floor and the transparent wall. Finally, the partial ground effect was tested with the same transparent surface. In these tests, the rotor was changed in height and the edge of the transparent wall was moved in radial direction of the rotor, Figure 6. This is an important study since during the first stages of the helicopter recovery in a frigate, its rotor is placed partially over the water and part over the flight deck. That causes an asymmetrical ground effect and can affect the helicopter performance during the maneuver generating unbalanced forces and a possible rollover torque.

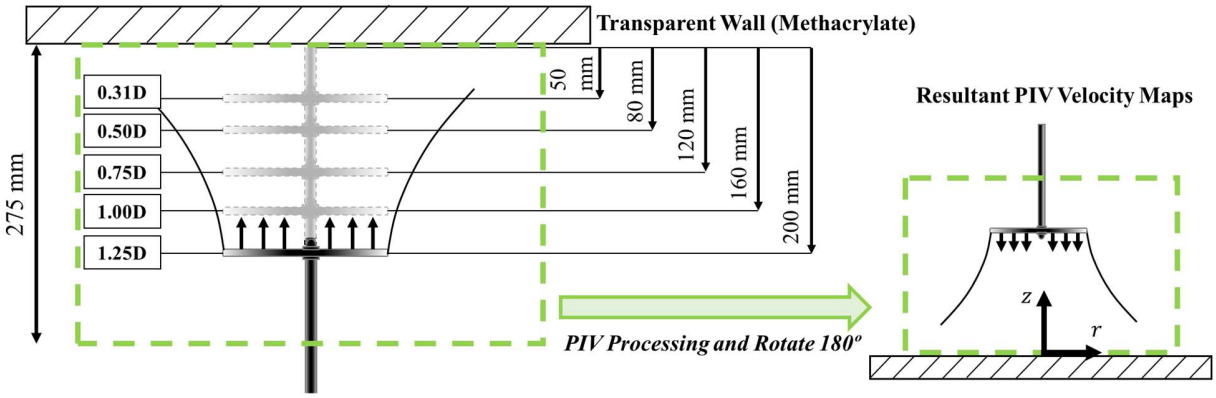



**Fig. 5 Diagram of rotor and wall aerodynamic interaction tests performed.**

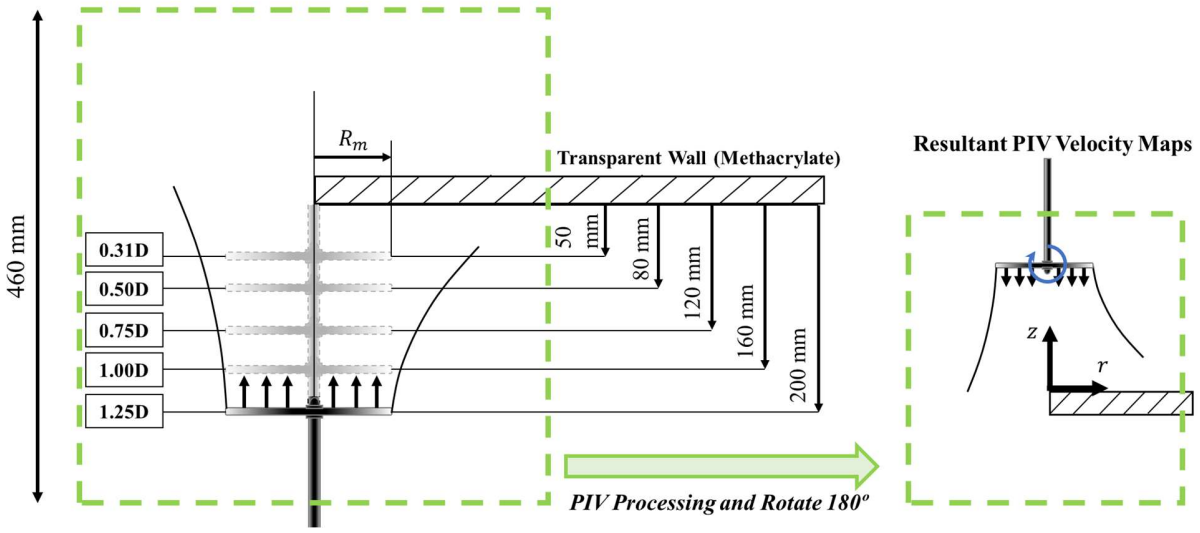



**Fig. 6 Diagram of rotor and partial wall aerodynamic interaction tests performed.**

### E. Rotor-frigate interaction

Finally, the last testing phase was carried out to obtain the flow produced by a rotor working over a frigate during its recovery phase. This recovery phase can be performed using various maneuvers. In the current tests, the stern maneuver has been used, as shown in Figure 7.

The military frigate model used for the tests is a 1:100 scaled model with a total length of 1.38 m. It represents the part above the waterline and has two prismatic blocks between the bow and stern deck, representing the frigate' superstructure. They correspond to the captain's bridge and the helicopter hangars.

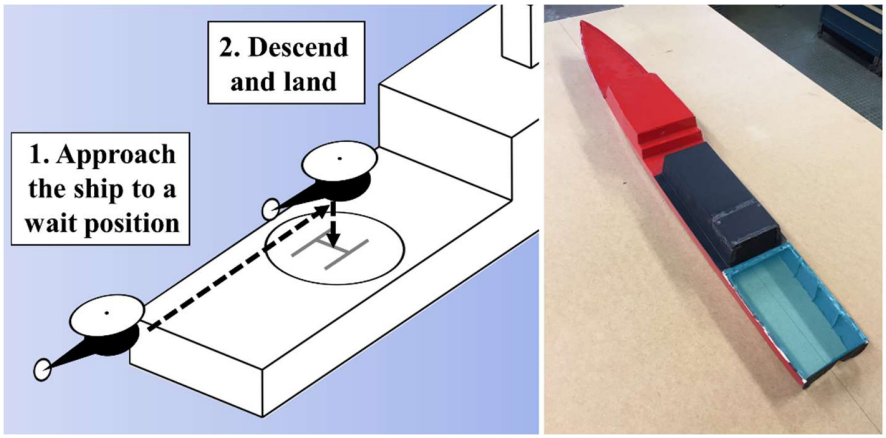



**Fig. 7 Helicopter performing a recovery operation over a frigate flight deck (left) and 1:100 frigate model used for the tests (right).**

The experimental set-up was similar to the previous tests with the rotor installed inverted. Due to this reason, all the experimental set-up had to be inverted also, Figure 8b. The model of the frigate used was fixed to a wooden wall of 2.24 m × 1.22 m, which represents the sea surface. This wall had a 0.6 m × 0.6 m hole where the frigate stern is placed in order to install a methacrylate flat plate integrated with the rest of the wood surface, Figure 8a. Finally, in order to allow the laser light to cross the aft-deck frigate surface, the metal plate of the flight deck of the frigate model was replaced by another transparent surface of methacrylate.

A last component of the assembly was the supports for the assembly of the wooden floor and the frigate model. This was made of welded metal profiles, fixed far enough from the model to avoid aerodynamic interferences during the measurements. As the rotor is fixed to the test section floor, to simulate the different positions of the helicopter rotor during the maneuver, the frigate model and its associated floor had to be moved on each test. Three positions of the rotor were studied at the same height of 50 mm above the frigate (Figure 8 c1 and c2). The first one (1) is when

the rotor is out of the frigate, the second one (2) is when the rotor is hovering half over the frigate and half over the sea and the last one (3) when the rotor is placed over the landing spot at the flight deck. Photographs taken during experimental tests of rotor and frigate interaction are shown in Figure 9.

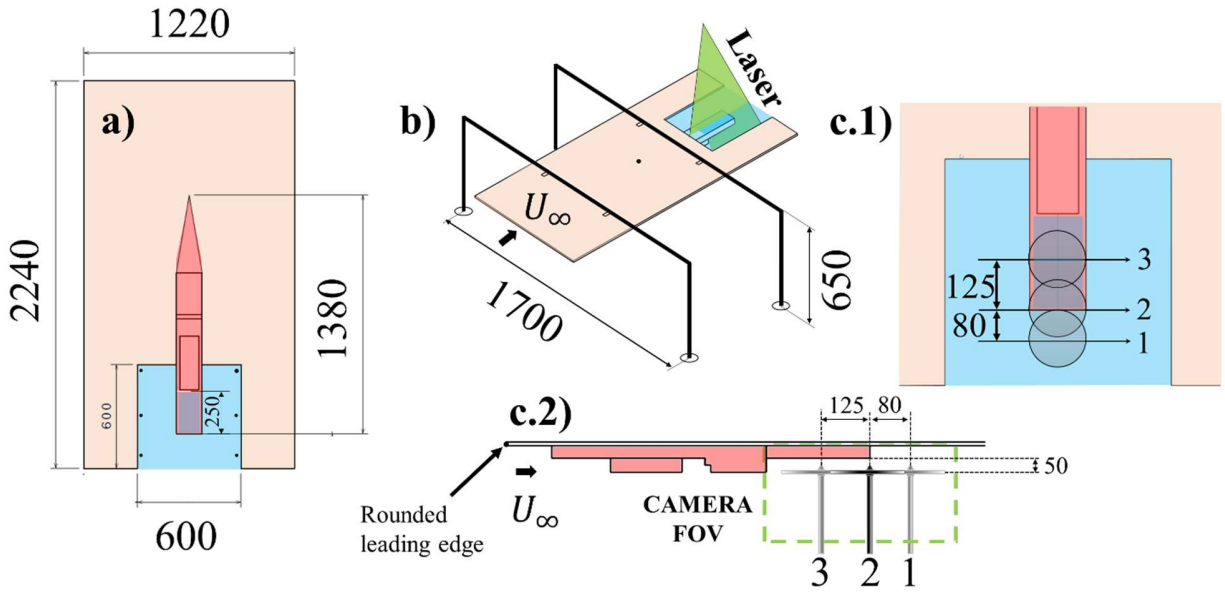



**Fig. 8 a) Dimensions of the wooden floor, frigate and methacrylate flat plate. b) Full-assembly of the experimental set-up. c.1) Positions of the helicopter rotor studied at the tests. c.2) Rounded leading edge of the board and camera field of view for PIV maps. All dimensions in millimeters (mm)**



**Fig. 9 Full experimental set-up for rotor and frigate aerodynamic interaction tests.**

## IV. Results

The experimental set-up was made with an inverted configuration. All the maps presented in this section have been post-processed and rotated 180 degrees, to improve understanding presenting them in the right way that a helicopter rotor usually works in a real case.

### A. Isolated Rotor, wall interaction and ground effect

Figures 10 and 11 show the velocity maps obtained when the rotor is working isolated (without free-stream velocity and objects nearby).

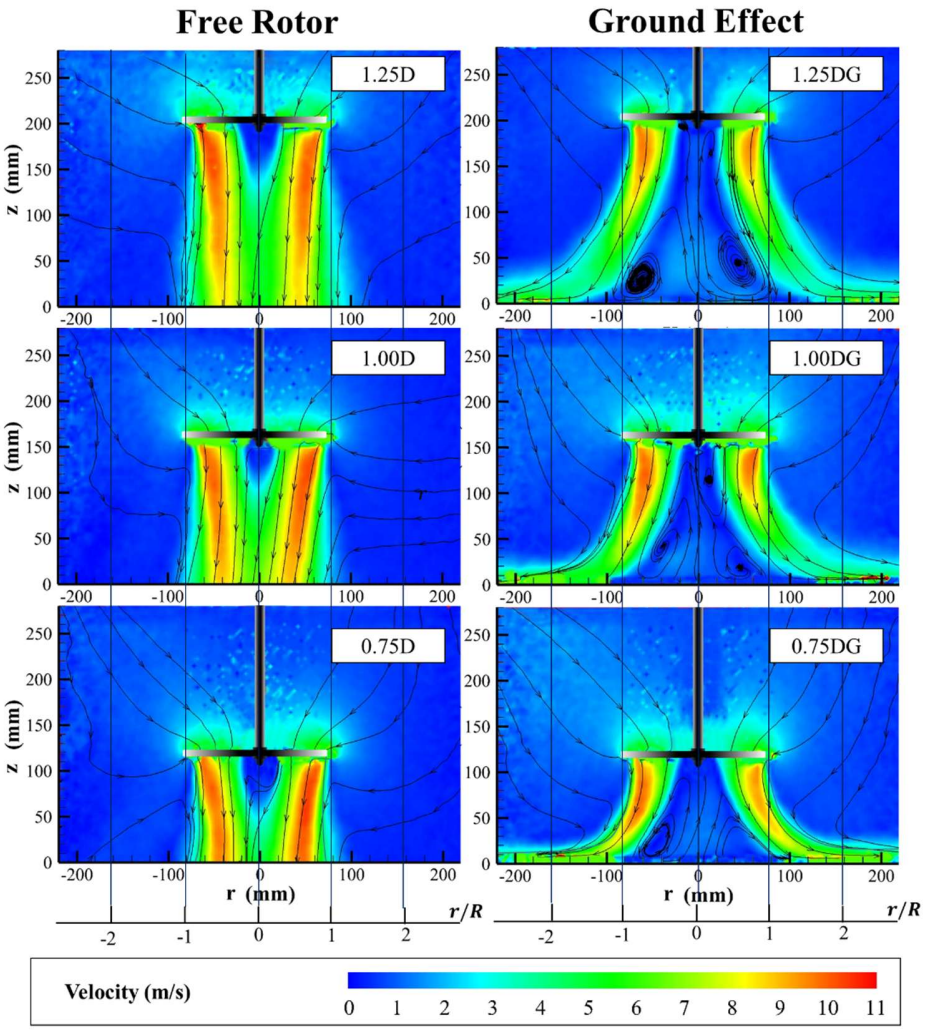



**Fig. 10 Velocity maps obtained from isolated rotor tests (left) and rotor and wall interaction tests (right). Rotor heights of 1.25D, 1.00D, and 0.75D.**

The velocity maps presented on the right side correspond to the same case but when there is a wall (or ground, G) placed at $z = 0$ mm. The rotor heights to the ground tested were 200 mm, 160 mm, 120 mm, 80 mm and 50 mm, which corresponds to 1.25D, 1.00D, 0.75D, 0.50D and 0.31D, where $D = 160$ mm is the rotor diameter.

For all no ground cases, the downwash propelled by the rotor descends vertically. Above the rotor, streamlines are curved, and the flow is accelerated until it passes through the rotor model. Once the flow has passed the blades, it reaches a higher velocity, the red areas of the velocity maps. The part of the downwash accelerated by the blades' tip, i.e. on the sides of the jet in the velocity maps at $r = -80$ mm and $r = 80$ mm, does not experience such acceleration and reaches lower velocity values (green zones). This is due to the interaction of the tip vortex, the interaction with the zero-velocity flow out of the jet and the contraction of the wake as predicted by momentum theory.

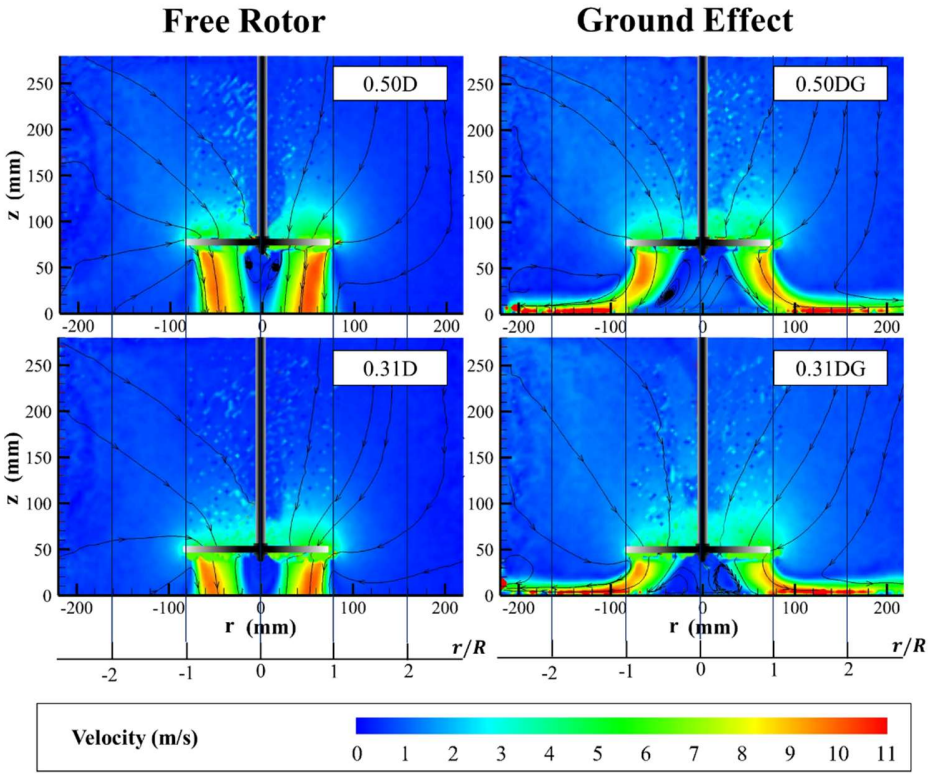



**Fig. 11 Velocity maps obtained from isolated rotor tests (left) and rotor and wall interaction tests (right). Rotor heights of 0.50D and 0.31D.**

Just on the rotor hub ($r = 0$ mm), there is a low-velocity area. However, it is only necessary to descend 50 mm in the $z$ coordinate so that this region of low-velocity disappears due to the union of the high-speed zones of the

downwash mentioned before. Observing the cases of the rotor with the presence of the ground (DG cases), the flow approach above the rotor is slightly decreased as expected.

The ground substantially modifies the flow below the rotor. Again, there is an acceleration of the flow by the rotor blades. But this time, the wake does not merely convect vertically. The streamlines are curved and separated to opposite sides due to the ground presence. In addition, the small low-speed region located under the transmission shaft now occupies a much larger area due to the observed downwash separation. It is also of interest to highlight the relatively high radial flow velocities close to the ground. They are related with the safety of ground personnel and loose objects on the ground.

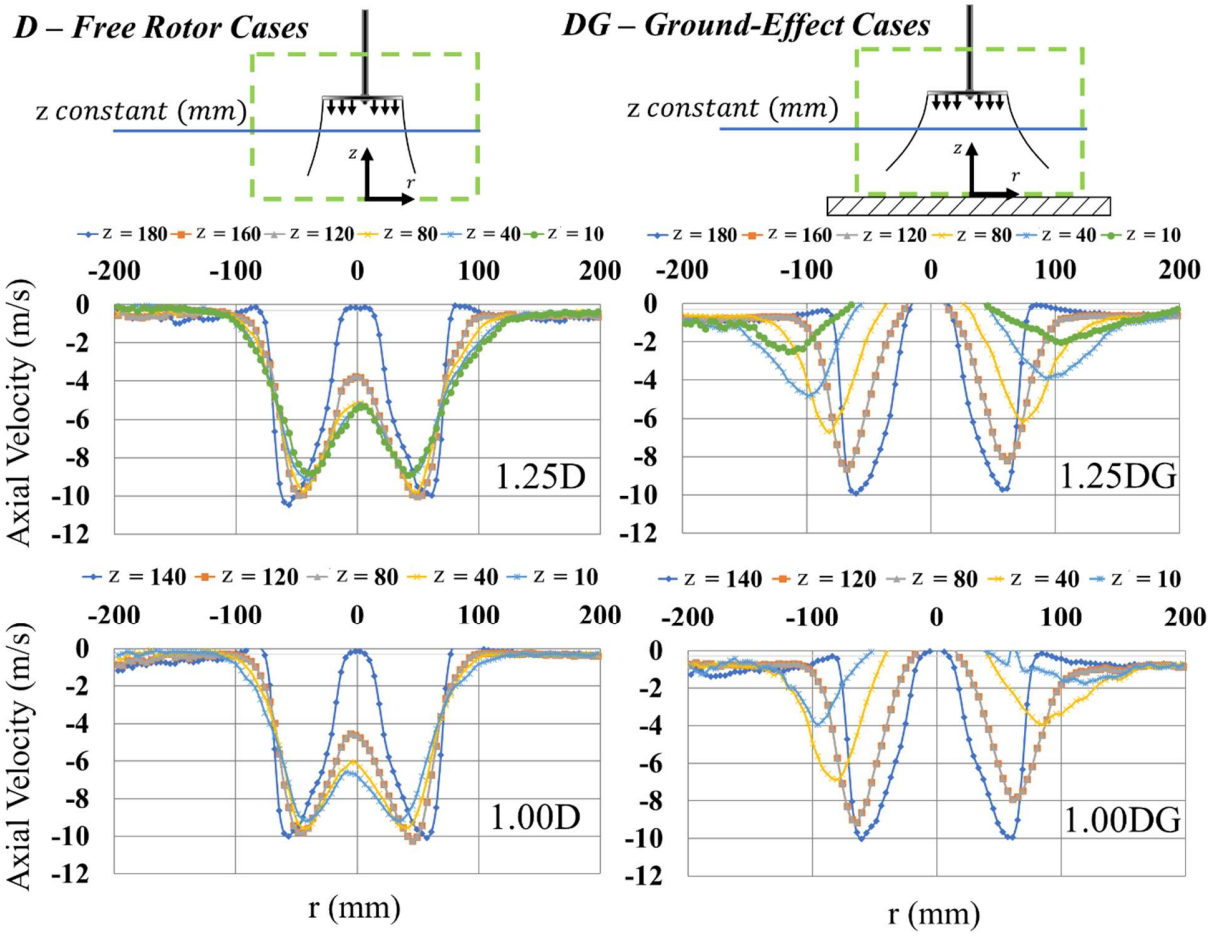



**Fig. 12 Velocity profiles of $z$ = constant lines below the rotor, placed at heights 1.25D and 1.00D, and with ground effect at 1.25DG and 1.00DG**

Once velocity maps have been presented, it is possible to obtain different velocity profiles of the induced velocity $v_{io}\ (r)$ along horizontal lines ($z = \text{constant}$) in any case, Figures 12 and 13. These velocity profiles show the same trends that have been seen on the previous velocity maps and they are useful to obtain averaged induced velocities.

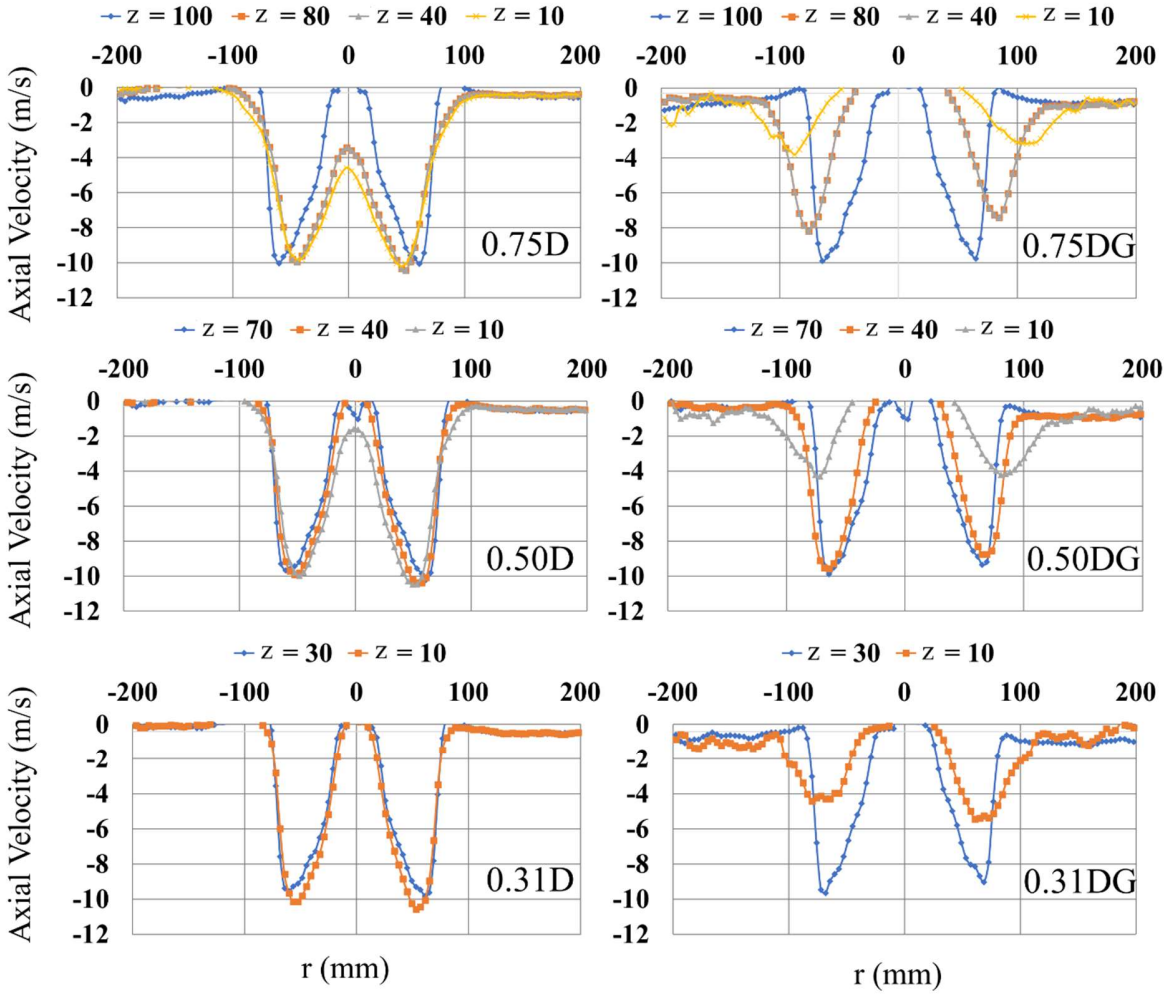



**Fig. 13 Velocity profiles of $z = \text{constant}$ lines below the rotor, placed at heights 0.75D, 0.50D and 0.31D and with ground effect at 0.75DG, 0.50DG and 0.31DG.**

**Table 2: Averaged mean axial velocity by the rotor at different cases of the two closest velocity profiles to the rotor.**

| | 1.25D | 1.25DG | 1.00D | 1.00DG | 0.75D | 0.75DG | 0.50D | 0.50DG | 0.31D | 0.31DG |
|---|---|---|---|---|---|---|---|---|---|---|
| $V_{io}$ (m/s) | 7.11 | 5.26 | 6.75 | 5.28 | 7.12 | 5.74 | 7.21 | 5.67 | 6.98 | 5.40 |

For the free rotor, the velocity profiles show that the jet propelled by the rotor does not expand in the $r-$ axis, as all curves become zero at practically the same values of $r$. The maximum peak of velocity is reduced as the velocity profiles represented are farther away from the rotor (lower $z$ coordinate). This is because both sides of the downwash are dissipating the energy and mixing to make the zero-velocity area disappear by $r = 0$ mm. This is a result of the wake contraction due to the momentum. For the ground effect velocity profiles at the right, the curves placed next to the rotor model (higher $z$ coordinate) are similar to those for the case without ground. However, as the velocity profiles are closer to the ground, their velocity peak decrease and the jet opens or widens, reaching higher values of $r$. Finally, with these velocity profiles the averaged induced axial velocity is presented in Table 2. To improve the results, only the two velocity profiles closest to the rotor were used. This means a maximum distance of 40 mm from the rotor model.

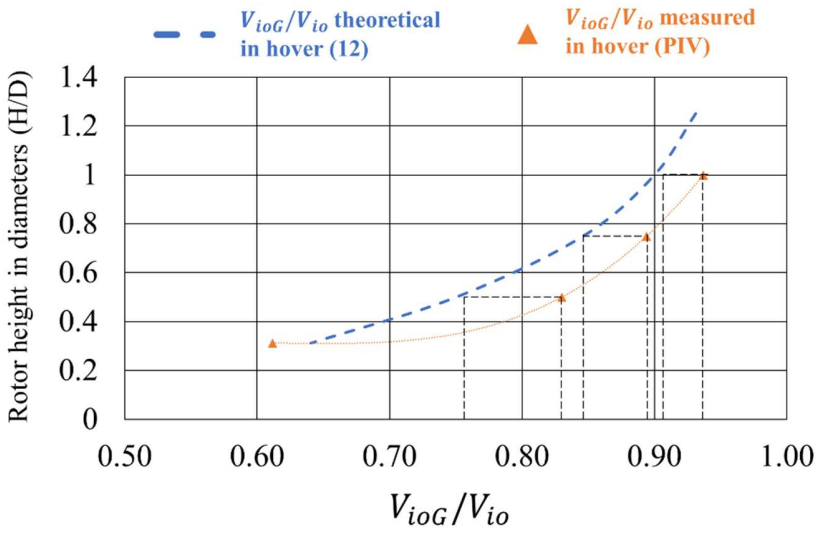



**Fig. 14 Induced axial velocity ratio for test cases studied**

In the proximity of ground, the power required for hovering must be smaller and the induced velocity decreases progressively with the ground proximity [33] according to the equation,

$$\frac{V_{ioG}}{V_{io}} = 1 - \frac{0.5}{1 + 4\left(\frac{H}{R}\right)^2} \tag{12}$$

where $V_{io}$ is the axial induced velocity without ground effect, $V_{ioG}$ is the axial induced velocity with ground effect, $H$ is the rotor height and $R$ is the rotor radius. The results of the experiments contained in Table 2 have been compared graphically with the theoretical of equation (12) in Figure 14, showing maximal differences of 0.08 $V_{ioG}/V_{io}$ for $Y = 0.5D$.

With the previous velocity maps in Figures 10 and 11, velocity difference maps between the isolated rotor and rotor-ground interference maps have been obtained for each height in Figure 15. In this figure is easy to see and quantify how the ground presence modifies the flow under the rotor and the curvature of the jet downstream. Red areas indicate where the downwash stream was placed for the no ground rotor tests and blue areas indicate where it is placed when the rotor is near to the ground. It has also been marked with dashed lines the shear layer between the downwash and the external flow for the case of the free rotor (black) and ground-effect rotor (red).

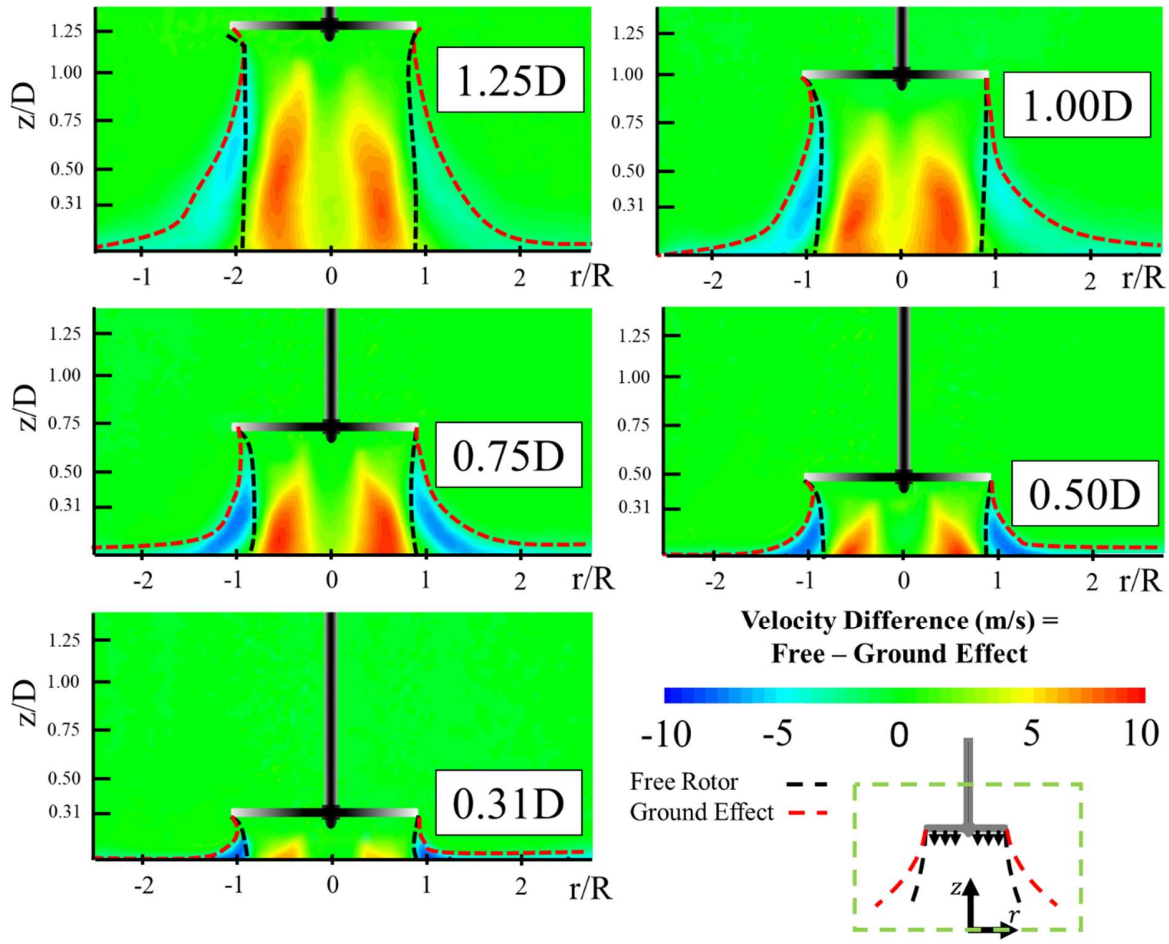



**Fig. 15 Velocity difference maps between isolated rotor model and rotor-wall interference.**

The shear layers have also been plotted for the different cases of ground effect in Figure 16, left. The heights are shown in rotor diameters ($z/D$) of the rotor and the horizontal axis in rotor radius ($r/R$). It should be noted that since the rotor is an axisymmetric problem, an increase in the jet width of 2 radius means a fourth time increase in the affected area by the jet on the ground.

The downwash deflection has also been measured with a parameter that measures the increase of jet width in radius (R) per unit of height in diameters (D),

$$\frac{\Delta R}{(z/D)} = \frac{\left(\frac{r}{R}\right)_{\frac{z}{D}=0.15} - 1}{\left(\frac{z}{D}\right)_{z=rotor}} \tag{13}$$

For example, a rotor at 0.50D from the ground increases the width of the jet by one radius for each diameter of height, Figure 16 right. There is a maximum of jet curvature for the case 0.75DG.

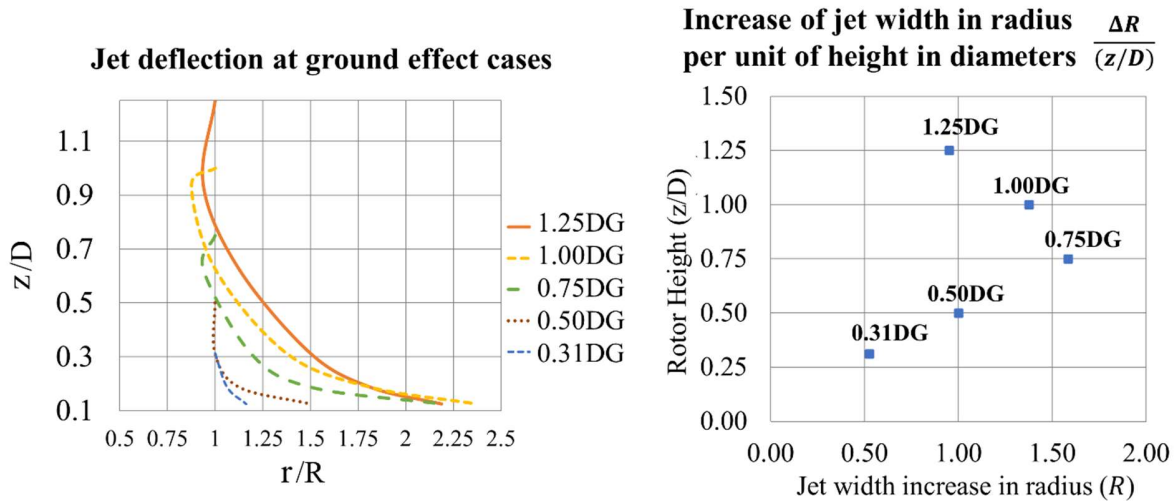



**Fig. 16 Jet deflection at different ground effect cases tested (left) and increase of jet width in radius per unit of height in diameters (right).**

### B. Partial Ground Effect

The results of partial ground effect at different rotor heights can be seen in Figure 17. They are important since when the helicopter rotor is approaching to the frigate before the landing, during a critical part of the maneuver, it flies with half of the rotor above the sea and the other half above the flight deck, affected by ground effect. This causes asymmetries in the flow and can lead to dangerous instabilities. The velocity maps obtained show a rotor with a

downwash affected by the ground presence. The half part of the rotor wake over the ground is deflected at the five heights tested, as expected.

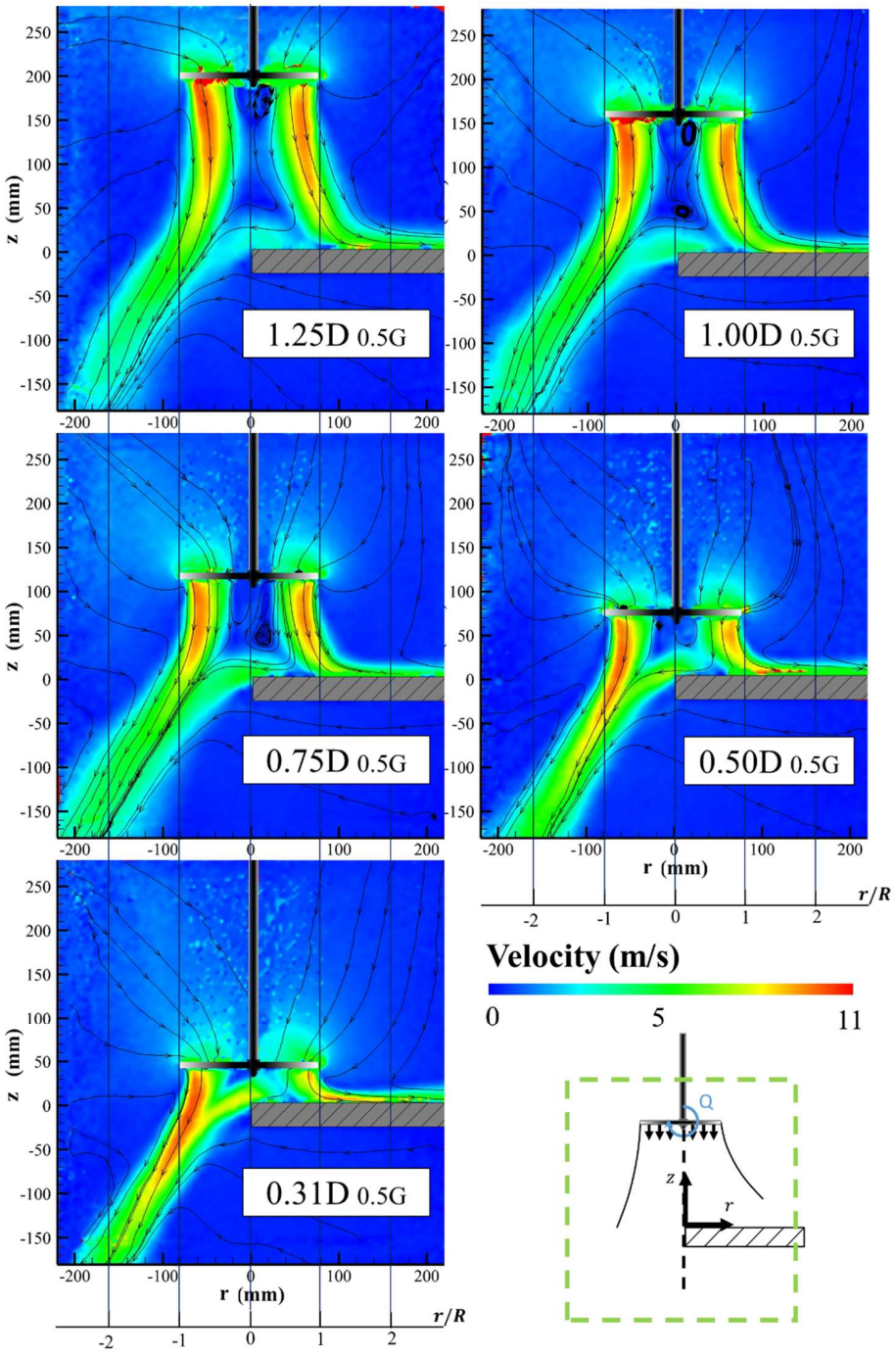



**Fig. 17 Velocity maps obtained from half ground effect distance (0.50G) below the rotor at different heights 1.25D, 1D, 0.75D, 0.5D and 0.31D.**

However, the other half part of the rotor that is hovering without the wall is also affected and its downwash is also curved to the opposite side of the wall. It is possible to conclude that the jet curvature over the free part of the rotor is practically the same in all cases. The lower the altitude at which the rotor is hovering, the bigger the interaction between each side of the wake of the jet. This can be observed at heights 0.50D and 0.31D, where the accelerated flow on the part over the ground escapes to the left side and joins to the free flow (streamline $r = 0$ mm and $z = 10$ mm). Note that the stagnation point underneath the rotor, where a recirculation area is generated, is always at a constant height with respect to the ground ($z = 50$ mm) for cases 1.25D, 1.00D, 0.75D, 0.50D.

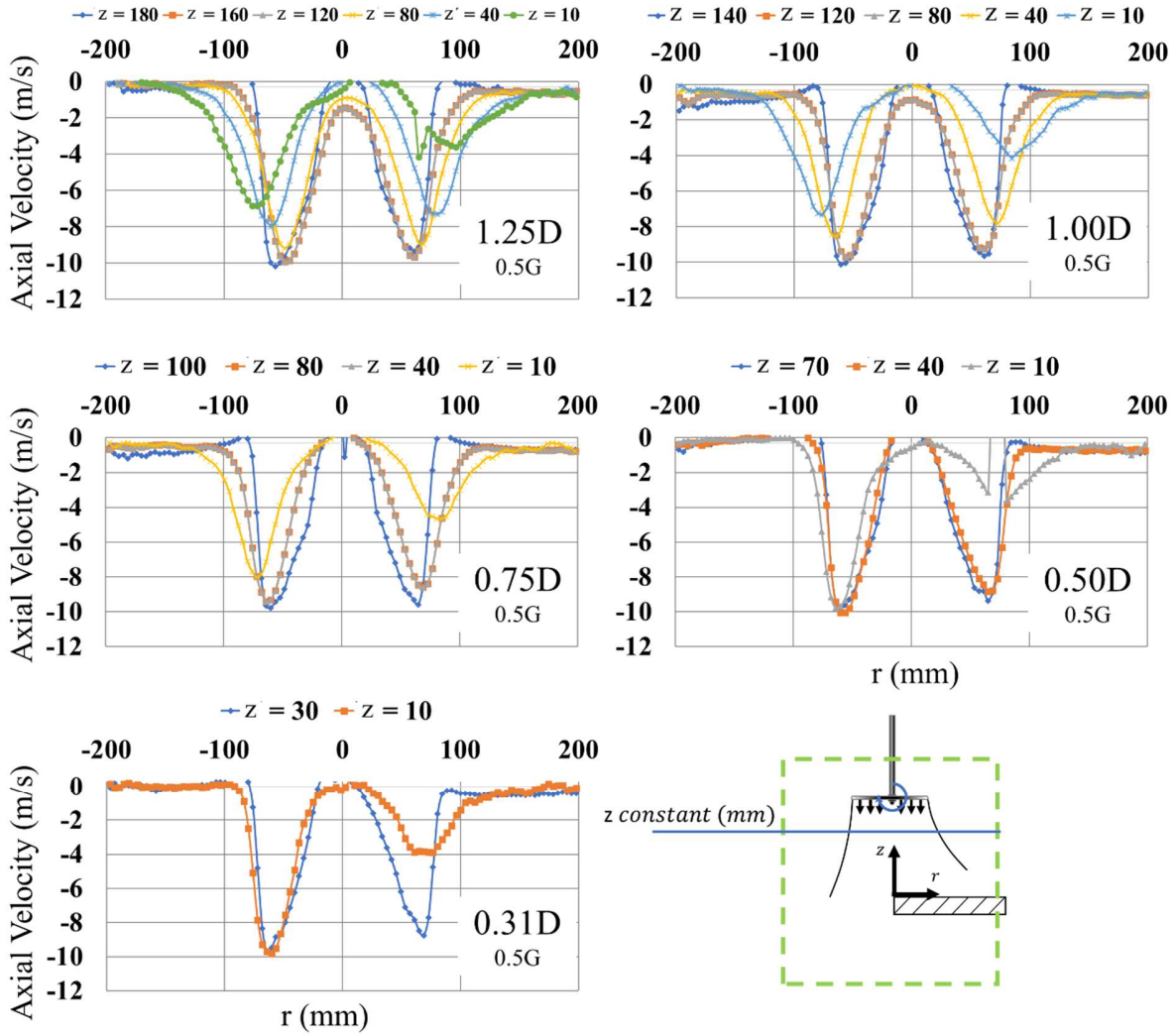



**Fig. 18 Velocity profiles of horizontal lines $z$ = constant below the rotor at the cases with partial ground effect (0.5G)**

Again, Figure 18 shows the axial velocity profiles for $z =$ constant lines. This time the curves are not symmetrical. The closer they are to the ground, the lower axial velocity peaks they have. The asymmetries and their relative change could affect the pilot workload during the maneuvers. To quantify the rotor downwash asymmetries generated by the ground presence, all the previous induced velocity profiles were used. The area defined by each profile can be obtained as,

$$A_L = \int_{-R}^{0} v_{io}(r)\, dr \qquad A_R = \int_{0}^{R} v_{io}(r)\, dr \tag{14}$$

where $A_L$ and $A_R$ are the areas under the profiles of the left ($r < 0$ mm) and right sides ($r > 0$ mm), $v_{io}(r)$ is the induced axial velocity, $r$ is the radial coordinate in rotor radius direction, defined in Figure 19 a). The averaged asymmetry parameter can be obtained with the following expression,

$$A = \frac{A_R - A_L}{A_R + A_L} \times 100 \tag{15}$$

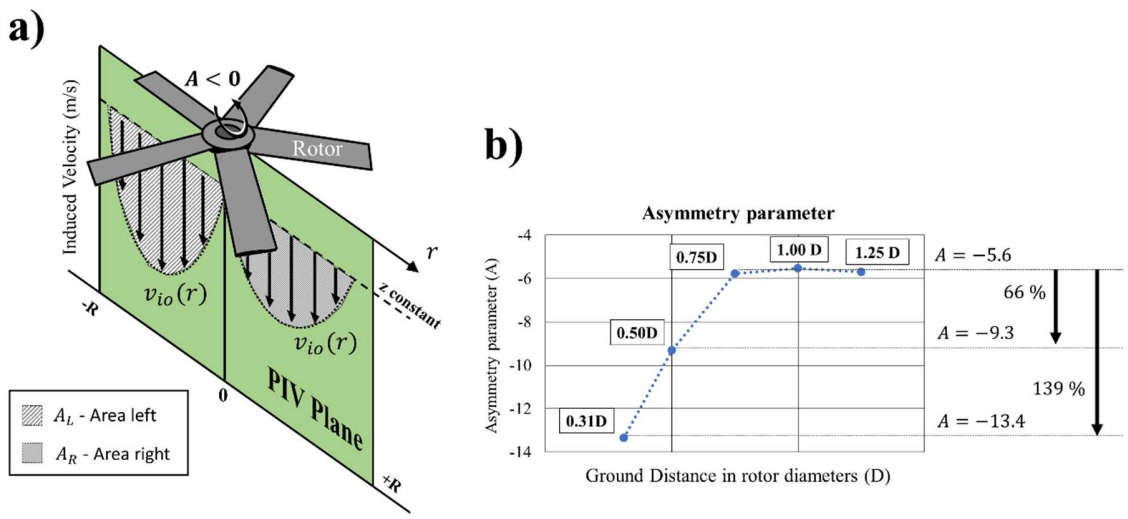



**Figure 19. a) $z$ constant line of velocity profiles on PIV Plane on the rotor downwash and areas to obtain asymmetry parameter (A). b) Assymetry parameter (A) values obtained from the partial ground effect cases tested.**

The parameter is negative ($A < 0$) when the induced velocities are higher at the left side of the rotor, which results in a tendency for the rotor to turn counterclockwise, Figure 19 a. In the same Figure 19 b, the averaged asymmetry parameter of all the profiles obtained for 1.25D, 1.00D, 0.75D, and 0.31D, is presented. The results confirm that the

closer the rotor is to the ground, the bigger asymmetries of the induced velocities are produced, especially with heights under 0.5 diameters (0.50D). Taking as reference the value $A = -5.6$ value obtained for the 1.00D case, the 0.50D case increases the rotor asymmetry by 66 % ($A = -9.3$) and the 0.31D case increases its asymmetry value to $A = -13.4$ (139 %).

### C. Rotor-Frigate Interaction

The last phase of the tests campaign was dedicated to quantify the aerodynamic effect of the rotor working over the aft flight-deck of a frigate. With the experimental set-up explained in section IV-E, the velocity maps obtained through PIV are shown in Figures 20 and 21. As the free-stream velocity is set in the wind tunnel ($U_\infty = 10$ m/s), the advance ratio is,

$$\mu = U_\infty / v_{tip_m} = 10 \,/\, 81.3 = 0.12 \tag{16}$$

The results of frigate interaction could be more accurate using a rotor model with trim capability. However, with the basic rigid rotor tested, the results can be quite similar to reality, since during the landing approach to the frigate the forward flight velocity is really low ($U_\infty = 10$ m/s), compared with the blade tip velocity ($V_{tip} = 80$ m/s).

During the first phase of the rotor approach to the frigate (Position 1, Figure 20), the rotor is still immersed in a flow with high-velocity, between 0.7 and 1, in non-dimensional values ($U/U_\infty$). That means that the rotor is working practically as it was in a $U_\infty = 10$ m/s free airstream. The downwash is deflected following the main flow direction and it does not interact with the frigate flight deck at the stern. If the rotor is affected by ground-effect, it only can be due to its interaction with the sea surface and not for the flight-deck surface.

The results are different when the rotor is hovering half over the flight deck and half over the sea (Position 2, Figure 20). In that position, the rotor is partially affected by the low-velocity area generated over the flight deck. The part of the rotor above the flight deck absorbs flow with less velocity than the other half. This means that the speed in the jets downstream of the rotor is not symmetrical on both sides. It reaches higher maximum values on the side that flies over the water. This asymmetry can lead to complex situations for the pilot during the maneuver.

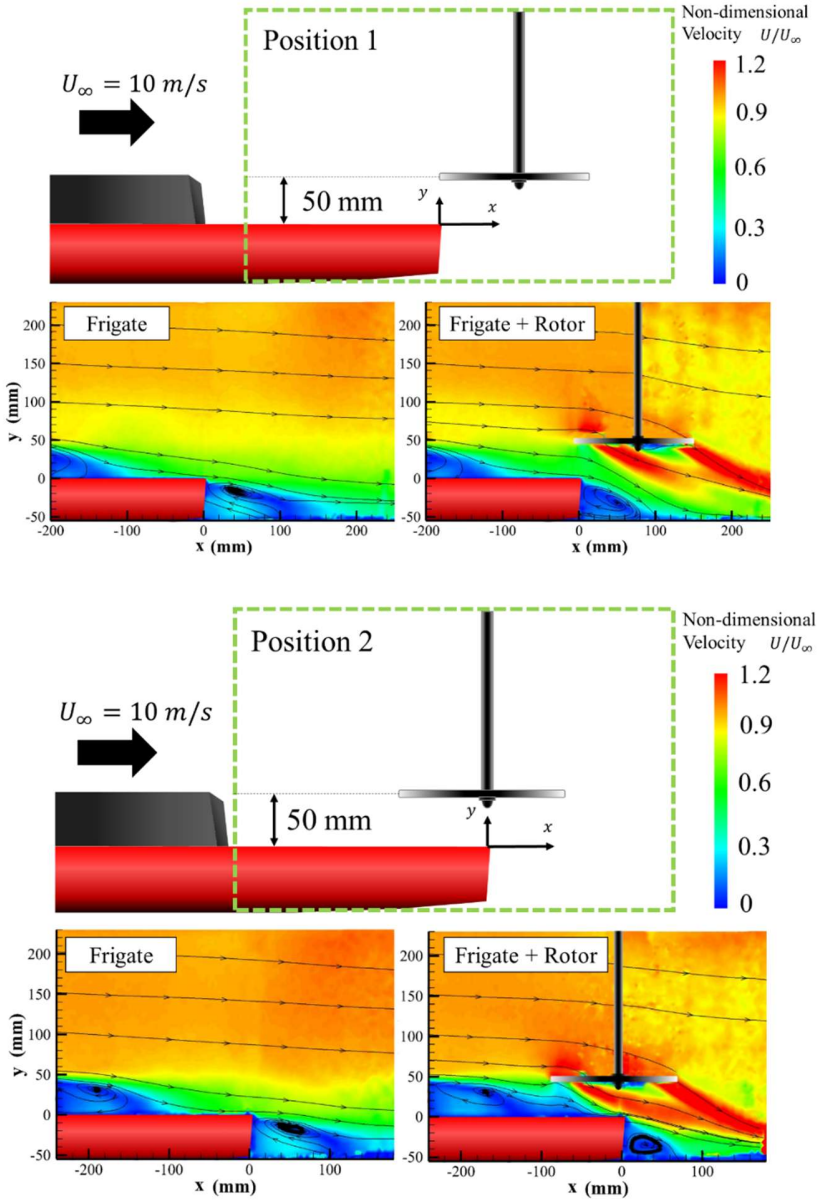



**Fig. 20 Velocity maps obtained when the rotor is making the approach maneuver over the helicopter flight deck at the stern. Positions 1 and 2.**

In Figure 21, when the rotor is working over the landing spot (position 3), the asymmetry of the airwake generated by the rotor is much more visible than in the previous case.

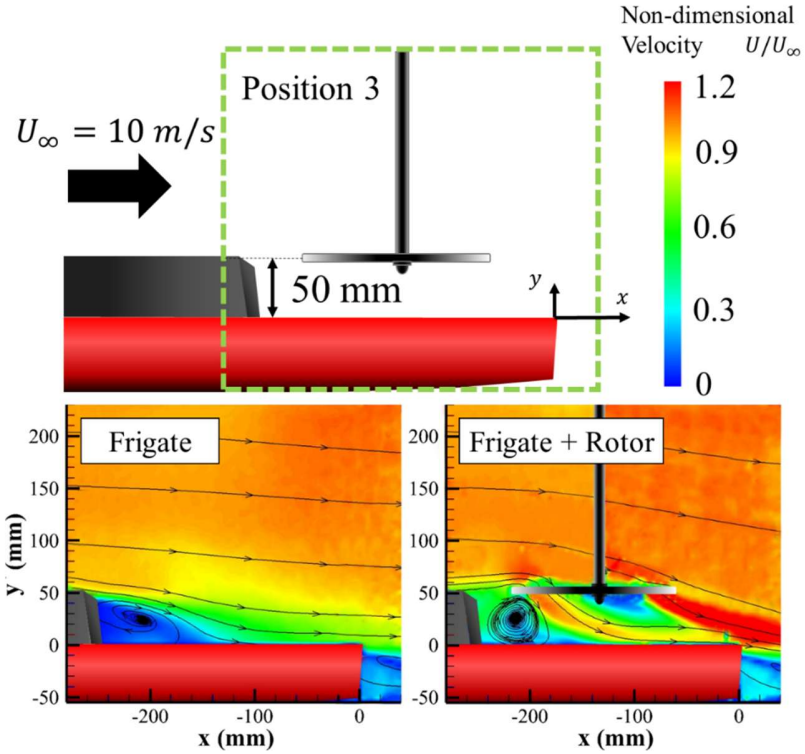



**Fig. 21 Velocity maps obtained when the rotor is making the approach maneuver over the helicopter flight deck at the stern. Position 3.**

At this critical point where the pilot must perform the final descent phase before the landing, the rotor is generating a wake that has a high-velocity gradient. Again, this may cause instabilities for the helicopter and difficult situations for the pilot to control the aircraft. In addition, the recirculation bubble generated behind the frigate's hangar is still present and is boosted by the rotor wake ($x = -220$ mm, $y = 30$ mm) while the rotor is working in that position.

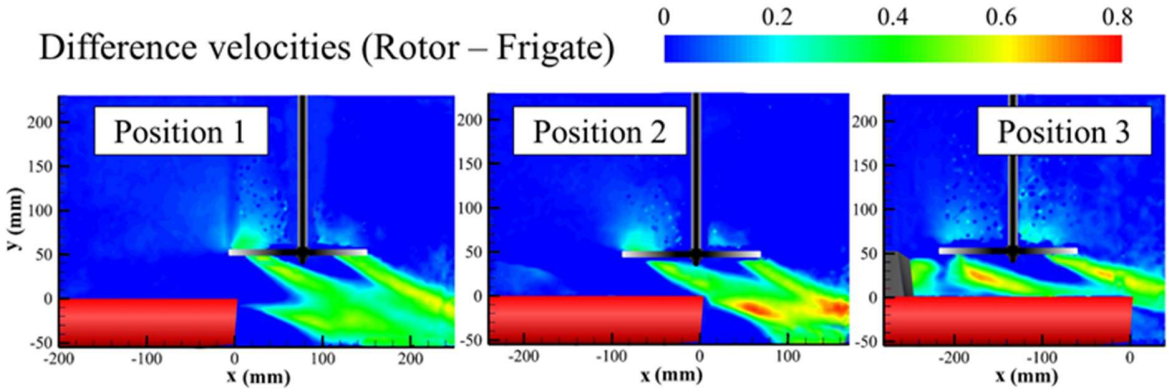



**Fig. 22 Maps of difference velocities of flow field with and without helicopter.**

Finally, the difference of velocities with and without helicopter are displayed in figure 22. The effect of the helicopter downwash on the frigate airwake is clearly visible. The wake of the rotor accelerates the flow downstream the frigate. At positions 1 and 2, the rotor affects the wake of the frigate generated by the flight deck, just above the sea surface ($x > 0$ mm). Position 3 accelerates the flow over the complete flight deck and recirculation region ($x < 0$ mm).

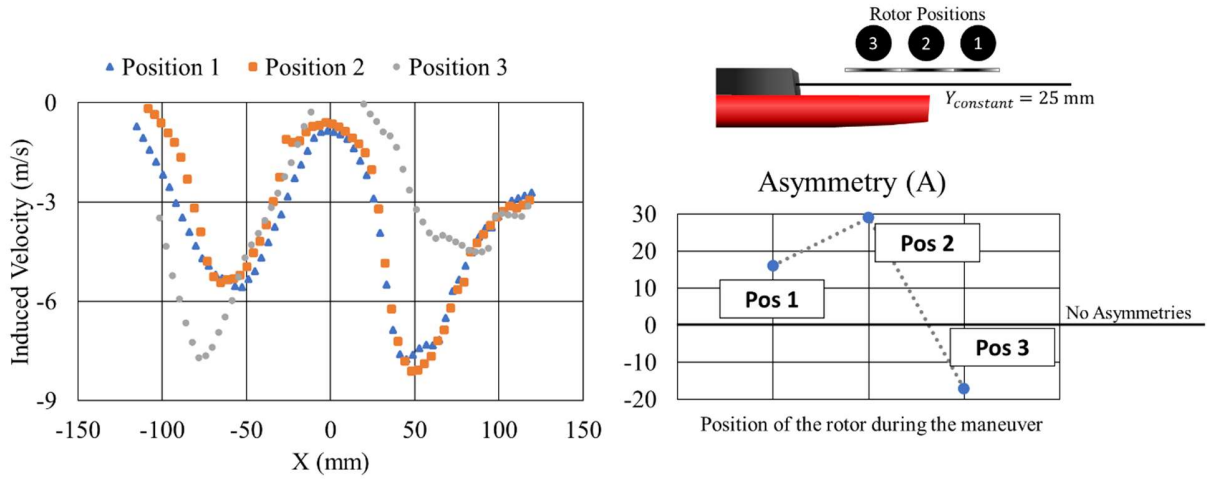



**Fig. 23 Velocity profiles at y = 25 mm from the deck in positions 1, 2 and 3 of the rotor. Asymmetry parameter (A) obtained for rotor positions 1, 2 and 3.**

Once the velocity maps have been described, the induced velocity profiles under the rotor and the associated asymmetry value obtained with equations (14) and (15) on a line $y_{constant} = 25$ mm, are presented in Figure 23. Both plots show that in the first position, the rotor downwash is quite asymmetrical ($A = 16$). The asymmetry increases by 40 % at the second position ($A = 29$). The worst situation comes at the final stage (position 3) of the landing approach. When the rotor is in position 3 the asymmetry parameter changes from positive to negative, up to $A = -17$. This means that in phases 1 and 2 the rotor has a tendency to rotate clockwise in the plane ($A > 0$) but when it hovers on the last position 3, the parameter is negative ($A < 0$) and the rotor has a tendency to rotate counterclockwise. This sudden change in flow behavior must increase the difficulty of the maneuver for the pilot. Note that the greater the asymmetries, the more pilot workload must be employed to perform a correct trimming of the rotor during the helicopter recovery process to a frigate.

## V.Conclusions

In this paper, a wind tunnel study with Particle Image Velocimetry (PIV) of a helicopter rotor model has been carried out. Velocity maps have been obtained from tests of the isolated rotor (no ground), and with the presence of a near-wall to study the ground effect at different rotor heights. The effect of the ground on the deflection of the downwash and on the rotor induced axial velocities by the rotor have been discussed. Additional velocity maps of partial ground effect when a helicopter rotor is hovering half over the ground have been also analyzed. This has been an important step to the study since the main goal was to analyze the landing maneuver of a helicopter above a frigate flight deck. The last part of the tests shows the aerodynamic effects of a rotor working above a flight deck of a frigate. The results have shown a decrease in the induced velocity when the helicopter is hovering in the ground-effect. High asymmetries in the airwake have been discovered in the partial ground effect tests. They are more important the closer the rotor is to the ground. An asymmetry parameter has been defined and calculated. It reaches asymmetries up to 1.39 times higher than when the rotor is far from the ground. Finally, the last tests performed have presented that during the landing approach of a helicopter to a frigate with stern wind, the rotor is affected by the flow over the flight deck only when it is hovering above the surface. During the first phases of the recovery maneuver, the rotor produces higher induced velocities on the right part than the left. However, this situation changes when the rotor hovers the last position of the maneuver, when the flow asymmetry calculated is inversed and the rotor has a tendency to turn counterclockwise. To sum up, the asymmetric flow generated by the rotor due the frigate airwake originated by the superstructure can lead to instabilities and risky situations for the helicopters' pilot during the real maneuvers. Due to these instabilities, the proper trim of the rotor can be a problem for the pilot, increasing his workload during this difficult maneuver.

In the future, it would be essential to study the same problem of helicopter and frigate interaction under different wind incident angles and analyzing different standardized maneuvers. Another improvement could be to use load cells to measure forces and moments of the rotor to estimate frequencies and relate them to the pilot's workload during the maneuver. In this study, steady cases were analyzed but a fast change of cyclic control input can indeed increase pilot workload more than reaching a certain level of steady cyclic control, and they could be detected by forces and moments measurements. Then, the text has been modified to say that although asymmetry and pilot workload are related, but not always directly.

It could also be important to introduce other effects such as different helicopter fuselages and also simulate the movement of the ship in different sea conditions.

## Acknowledgments

The authors would like to thank the staff of the Experimental Aerodynamics department of INTA who participated in the tests presented in this paper.

## References

[1] Kääriä, C., Wang, Y., White, M., and Owen, I., "An experimental technique for evaluating the aerodynamic impact of ship superstructures on helicopter operations", *Ocean Engineering*, Vol. 61, 2013, pp. 97-108. https://doi.org/10.1016/j.oceaneng.2012.12.052

[2] Wakefield, N., Newman, S., and Wilson, P., "Helicopter flight around a ship's' superstructure", *Proceedings of the Institution of Mechanical Engineers, Part G: Journal of Aerospace Engineering*, Vol. 216, No. 1, 2002, pp. 13-28. https://doi.org/10.1243/0954410021533391

[3] Rhoades, M., and Healey, J., "Flight deck aerodynamics of a nonaviation ship", *Journal of Aircraft*, Vol. 29, No. 4, 1992, pp. 619-626. https://doi.org/10.2514/3.46210

[4] Dooley, G., Krebill, A., Martin, J., Buchholz, J., and Carrica, P., "Structure of a Ship Airwake at Multiple Scales", *AIAA Journal*, Vol. 58, No. 5, 2020, pp. 2005-2013. https://doi.org/10.2514/1.J058994

[5] Thedin, R., Kinzel, M., Horn, J., and Schmitz, S., "Coupled Simulations of Atmospheric Turbulence-Modified Ship Airwakes and Helicopter Flight Dynamics", *Journal of Aircraft*, Vol. 56, No. 2, 2019, pp. 812-824. https://doi.org/10.2514/1.C035158

[6] Crozon, C., Steijl, R., and Barakos, G., "Numerical Study of Helicopter Rotors in a Ship Airwake", *Journal of Aircraft*, Vol. 51, No. 6, 2014, pp. 1813-1832. https://doi.org/10.2514/1.C032535

[7] Foeken, M., Pavel, M. D., "Investigation on the simulation of helicopter/ship operations". *Faculty of Aerospace engineering, Delft University of Technology*.

http://hdl.handle.net/20.500.11881/218

[8] Van Muijden, J., Boelens, O., van der Vorst, J., and Gooden, J., "Computational ship airwake determination to support helicopter-ship dynamic interface assessment", *21st AIAA Computational Fluid Dynamics Conference*, 2013. https://doi.org/10.2514/6.2013-3078

[9] Memon, W., Owen, I., and White, M., "Motion Fidelity Requirements for Helicopter-Ship Operations in Maritime Rotorcraft Flight Simulators", *Journal of Aircraft*, Vol. 56, No. 6, 2019, pp. 2189-2209. https://doi.org/10.2514/1.C035521

[10] Watson, N., Owen, I., and White, M., "Piloted Flight Simulation of Helicopter Recovery to the Queen Elizabeth Class Aircraft Carrier", *Journal of Aircraft*, 2020, pp. 1-19. https://doi.org/10.2514/1.C035733

[11] Van Muijden, J., Boelens, O., van der Vorst, J., and Gooden, J., "Computational ship airwake determination to support helicopter-ship dynamic interface assessment", *21st AIAA Computational Fluid Dynamics Conference*, 2013. https://doi.org/10.2514/6.2013-3078

[12] Shi, Y., Xu, Y., Zong, K., and Xu, G., "An investigation of coupling ship/rotor flowfield using steady and unsteady rotor methods", *Engineering Applications of Computational Fluid Mechanics*, Vol. 11, No. 1, 2017, pp. 417-434. https://doi.org/10.1080/19942060.2017.1308272

[13] Zhang, J., Minelli, G., Rao, A., Basara, B., Bensow, R., and Krajnović, S., "Comparison of PANS and LES of the flow past a generic ship", *Ocean Engineering*, Vol. 165, 2018, pp. 221-236. https://doi.org/10.1016/j.oceaneng.2018.07.023

[14] Yuan, W., Wall, A., and Lee, R., "Combined numerical and experimental simulations of unsteady ship airwakes", *Computers & Fluids*, Vol. 172, 2018, pp. 29-53. https://doi.org/10.1016/j.compfluid.2018.06.006

[15] Thedin, R., Murman, S., Horn, J., and Schmitz, S., "Effects of Atmospheric Turbulence Unsteadiness on Ship Airwakes and Helicopter Dynamics", *Journal of Aircraft*, Vol. 57, No. 3, 2020, pp. 534-546. https://doi.org/10.2514/1.C035643

[16] Ji, H., Chen, R., and Li, P., "Real-time simulation model for helicopter flight task analysis in turbulent atmospheric environment", *Aerospace Science and Technology*, Vol. 92, 2019, pp. 289-299. https://doi.org/10.1016/j.ast.2019.05.066

[17] Forsythe, J., Lynch, E., Polsky, S., and Spalart, P., "Coupled Flight Simulator and CFD Calculations of Ship Airwake using Kestrel", *53rd AIAA Aerospace Sciences Meeting*, 2015. https://doi.org/10.2514/6.2015-0556

[18] Forrest, J., Kaaria, C., and Owen, I., - “Determining the Impact of Hangar-Edge Modifications on Ship-Helicopter Operations using offline and Piloted helicopter Flight Simulation”, *American Helicopter Society 66th Annual Forum & Technology* Display, Phoenix, 2010.

[19] Forrest, J., Kaaria, C., and Owen, I., "Evaluating ship superstructure aerodynamics for maritime helicopter operations through CFD and flight simulation", *The Aeronautical Journal*, Vol. 120, No. 1232, 2016, pp. 1578-1603. https://doi.org/10.1017/aer.2016.76

[20] Bardera-Mora, R., Barcala-Montejano, M., Rodríguez-Sevillano, A., de Diego, G., and de Sotto, M., "A spectral analysis of laser Doppler anemometry turbulent flow measurements in a ship air wake", *Proceedings of the Institution of Mechanical Engineers, Part G: Journal of Aerospace Engineering*, Vol. 229, No. 12, 2015, pp. 2309-2320. https://doi.org/10.1177/0954410015573972

[21] Kääriä, C., Wang, Y., Padfield, G., Forrest, J., and Owen, I., "Aerodynamic Loading Characteristics of a Model-Scale Helicopter in a Ship's Airwake", *Journal of Aircraft*, Vol. 49, No. 5, 2012, pp. 1271-1278. https://doi.org/10.2514/1.C031535

[22] Silva, M. J., Yamauchi, G. K., Wadcock, A. J., Long, K. R., “Wind tunnel investigation of the aerodynamic interactions between helicopters and tiltrotors in a shipboard environment”. *4th Decennial Specialist’s Conference on Aeromechanics*, San Francisco, CA, 2004.

[23] Wadcock, A., Yamauchi, G., Heineck, J., Silva, M., Long, K. “PIV Measurements of the Wake of a Tandem-Rotor Helicopter in Proximity to a Ship”. *Conference on Aeromechanics, San Francisco, CA. January 21-23, 2004.*

[24] Stargel, D., and Landman, D., "A wind tunnel investigation of ship airwake/rotor downwash coupling using design of experiments methodologies", *50th AIAA Aerospace Sciences Meeting including the New Horizons Forum and Aerospace Exposition*, 2012. https://doi.org/10.2514/6.2012-767

[25] Lee, R., and Zan, S., "Wind Tunnel Testing of a Helicopter Fuselage and Rotor in a Ship Airwake", *Journal of the American Helicopter Society*, Vol. 50, No. 4, 2005, pp. 326-337. https://doi.org/10.4050/1.3092869

[26] Leishman, J., *Principles of Helicopter aerodynamics.* Cambride Aerospace Series. 2nd Edition, 2016.

[27] Adrian, R. and Westerweel, J. Particle Image Velocimetry. Cambridge: Cambridge University Press, 2001

[28] Adrian, R., "Particle-Imaging Techniques For Experimental Fluid-Mechanics", Annual Review of Fluid Mechanics, Vol. 23, No. 1, 1991, pp. 261-304.

[29] Prasad, A. K. “Particle image velocimetry”. CURRENT SCIENCE-BANGALORE-, Vol. 79, No. 1, 2000, pp. 51-60.

[30] Raffel, M. C., Willert, F., Scarano, C., Kähler, S. Wereley and J. Kompenhans. Particle Image Velocimetry. Springer. 2007

[31] Echols, W. H. and J. A. Young. “Studies of portable air-operated aerosol generators” (No. NRL-5929). *Naval Research Lab Washington DC*. 1963.

[32] Kähler, C., Sammler, B., and Kompenhans, J., "Generation and control of tracer particles for optical flow investigations in air", *Experiments in Fluids*, Vol. 33, No. 6, 2002, pp. 736-742. https://doi.org/10.1007/s00348-002-0492-x

[33] Petrovic, Z., Stupar, S. Kostic, I., Simonovic, A. “Determination of a Light Helicopter Flight Performance at the Preliminary Design Stage“. *Journal of Mechanical Engineering*, Vol 56, No. 9, 2010 pp. 535-543.